



Cite this: *RSC Adv.*, 2018, 8, 33717

Synthesis of interconnected mesoporous ZnCo₂O₄ nanosheets on a 3D graphene foam as a binder-free anode for high-performance Li-ion batteries†

Xu Wang, ^a Qi Chen,^a Pei Zhao ^{*b} and Miao Wang^{*a}

Interconnected mesoporous sheet-like ZnCo₂O₄ nanomaterials directly grown on a three-dimensional (3D) graphene film (GF) coated on Ni foam (NF) have been successfully synthesized *via* an effective chemical vapor deposition (CVD) method combined with a subsequent hydrothermal route. When the ZnCo₂O₄@3DGF@NF composite material with a high surface area of 46.06 m² g⁻¹ is evaluated as a binder-free anode material for lithium ion batteries, it exhibits a superior electrochemical performance with a high discharge capacity (1223 mA h g⁻¹ at a current density of 500 mA g⁻¹ after 240 cycles), and an excellent reversibility (coulombic efficiency of 97–99%). Such an outstanding electrochemical performance may be attributed to its unique mesoporous sheet-like nanostructure with a 3DGF supporting, which can facilitate the electrolyte penetration and accelerate the ion/electron transport, as well as buffer the volume variation during charge/discharge processes.

Received 12th June 2018
Accepted 24th September 2018

DOI: 10.1039/c8ra05035j

rsc.li/rsc-advances

Introduction

In the past few decades, lithium ion batteries (LIBs) have played a vital role in powering portable electronics, energy storage devices and even electric vehicles, in view of their advantages of outstanding specific energy density and stable cycling performance.^{1,2} Nevertheless, graphite as the present commercial anode material is difficult to further apply to high-performance LIBs due to its low theoretical specific capacity (372 mA h g⁻¹).^{3,4} Frankly, many efforts have been devoted to exploring high-capacity anode materials in order to replace graphite for next-generation LIBs.^{5–8} Significantly, a promising family of mixed transition-metal oxides (MTMOs) (designated as A_xB_{3–x}O₄; A, B = Co, Ni, Zn, Mn, Fe, *etc.*) have recently attracted increasing worldwide interest for their high theoretical capacity serving as anode materials.^{9–12} Among these MTMO materials, ZnCo₂O₄, which shows a great potential as an ideal anode material for LIBs on account of enhanced electrochemical activity, abundant raw materials and low toxicity, is of significant interest.^{13,14} Importantly, apart from the conversion reaction between Zn/Co species and Li usually observed in other MTMOs, the special alloying reaction between Zn and Li (LiZn alloy) also can contribute to additional lithium storage capacity.^{15–17} In consequence, the theoretical capacity of ZnCo₂O₄ is as high as 975 mA h g⁻¹, which is close to three times higher than that of

graphite. However, the use of ZnCo₂O₄ in high power LIBs is restricted which can be ascribed to the poor electrical conductivity and slow lithium ion diffusivity.^{18,19} More seriously, like other MTMO anode materials, ZnCo₂O₄ also suffers from a very problematic disadvantage of a short cycling life owing to pulverization, caused by a huge volume variation during the repeated charge/discharge processes.^{20,21}

Fortunately, smart design of nanostructured MTMOs has been regarded as a successful means to overcome the electron/ion diffusivity limitations by shortening the diffusion path. In addition, the nanostructured electrode materials also could well accommodate the volume variation during Li⁺ insertion/extraction. The ZnCo₂O₄ nanomaterials with various architectures have been synthesized and evaluated as energy storage materials, such as nanowires,²² nanosheets,^{23,24} microspheres^{25,26} and other novel nanostructures,^{27–29} *etc.* However, these above mentioned nanomaterials must be mixed with conductive additives and polymer binders to form a slurry and then fastened to current collectors, which may impair the specific electrode capacity, and give rise to aggregation of nanomaterials.^{30,31} To well circumvent these issues, it is thus logical to build a binder-free electrode by directly growing self-supported nanostructured active materials on a conductive substrate.^{30,32,33} As is well known, graphene has some advantageous characteristics, including excellent chemical inertness, high electrical conductivity and specific surface area, good flexibility, which is regarded as an ideal conductive support for electrochemical performance improving of MTMOs.^{34,35} Besides, Ni foam is an excellent substrate to grow three-dimensional porous materials on account of its 3D interconnected character.^{36,37}

^aDepartment of Physics, Zhejiang University, Hangzhou 310027, P. R. China. E-mail: miaowang@zju.edu.cn; peizhao@zju.edu.cn

^bInstitute of Applied Mechanics, Zhejiang University, Hangzhou 310027, P. R. China

† Electronic supplementary information (ESI) available. See DOI: 10.1039/c8ra05035j



From the above discussion, herein, we demonstrate a composite electrode with a three-dimensional structure, comprised of mesoporous sheet-like ZnCo_2O_4 materials supported on a 3D graphene film (3DGF) coated on the Ni foam matrix, which is shown in Scheme 1. The 3DGF composed of multilayer graphene sheets is deposited on a Ni foam (denoted as 3DGF@NF) *via* a chemical vapor deposition method. Subsequently, the ZnCo_2O_4 materials grown on the graphene substrate (denoted as ZnCo_2O_4 @3DGF@NF) are prepared through a facile hydrothermal strategy, followed by an annealing treatment. Our synthesized ZnCo_2O_4 @3DGF@NF composite material is further evaluated as the electrode for LIBs by assembling half cells and exhibited a remarkable reversible capacity, superior rate capability and a long cycling life.

Experimental details

Synthesis of three dimensional graphene film (3DGF)

The graphene film was prepared by the chemical vapor deposition (CVD) method. Briefly, the Ni foam was loaded into a quartz tubular furnace, wherein the protective Ar gas (200 sccm) flow was fluxed while ramping the temperature up to 1000 °C within 60 min. After stabilization of the temperature, the Ni foam was firstly cleaned under the mixed gas flow of Ar (400 sccm) and H_2 (100 sccm) for 5 min to remove the contaminated oxide layers coated on the surface of Ni foam. Subsequently, the targeted CH_4 gas flow (30 sccm) as the carbon source was introduced into the tubular furnace for 3 min accompanied with protective mixed gas flow of Ar (200 sccm) and H_2 (50 sccm) in order to deposit graphene film on Ni foam. Ultimately, the quartz tubular furnace was rapidly cooled down to room temperature without a delay with the uninterrupted protection of mixed gas flow of Ar and H_2 .

Synthesis of ZnCo_2O_4 nanosheet arrays@3DGF@NF

All the chemicals used in the experiments were of analytical grade and used as received. In a typical procedure, 1 mmol $\text{Zn}(\text{NO}_3)_2 \cdot 6\text{H}_2\text{O}$, 2 mmol $\text{Co}(\text{NO}_3)_2 \cdot 6\text{H}_2\text{O}$, and 12 mmol urea were dissolved in 30 ml deionized water to form a homogeneous solution after magnetic stirring for 15 min. Then the as-prepared solution and a piece of 3DGF@NF (3 cm \times 2 cm) were transferred together into a 50 ml Teflon-lined stainless-steel autoclave and heated at 120 °C for 6 h. After cooling down to ambient temperature, the synthesized product was taken out and rinsed several times with deionized water and ethanol, followed by calcination at 400 °C for 3 h in air

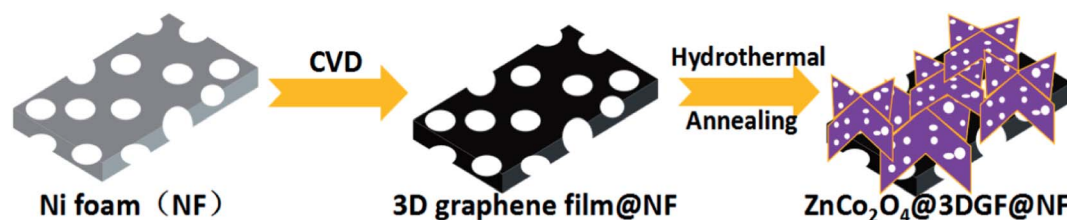
atmosphere at a ramping rate of 2 °C min^{-1} . As a comparison, ZnCo_2O_4 arrays directly grown on Ni foam substrate (ZnCo_2O_4 @NF) without supporting graphene were also prepared in the same procedure. In addition, ZnCo_2O_4 powders were collected from the solution after hydrothermal reaction by using a high-speed centrifuging method, followed by the same calcination process.

Materials characterizations

The crystalline structure and compositional nature of synthesized products were investigated by a combination of X-ray diffraction (XRD) (bruker D8 ADVANCE), X-ray photoelectron (XPS) (Escalab250Xi) and Raman spectroscopy (LabRAM HR Evolution, 532 nm excitation wavelength), respectively. The morphology and microstructure studies were conducted by using field emission scanning electron microscopy (FESEM, Utral 55) with an energy dispersive X-ray spectrometer (EDS), and transmission electron microscopy (TEM, JEM-2100HR). The N_2 adsorption/desorption isotherms were performed on an AUTOSORB-IQ2-MP instrument to measure the BET surface area of the products.

Electrochemical measurement

Electrochemical experiments were carried out using the standard CR2025 coin-type cell with a lithium disk (Φ 16 mm) as a counter/reference electrode, our synthesized composite materials as a working electrode, and a Celgard 2400 polypropylene film (Φ 19 mm) as a separator soaked with 1 M LiPF_6 in EC : DEC : DMC (1 : 1 : 1, v/v/v) nonaqueous electrolyte. All cells were assembled or disassembled in an Ar-filled glove box ($\text{O}_2 < 0.5$ ppm, $\text{H}_2\text{O} < 0.5$ ppm). The ZnCo_2O_4 @3DGF@NF and ZnCo_2O_4 @NF composites were cut into 1.0 cm \times 1.0 cm dimensions, respectively, which were directly used as the working electrode without any conductive additive and polymer binder. The typical loading mass of ZnCo_2O_4 was around 0.85 mg cm^{-2} and 1.0 mg cm^{-2} in ZnCo_2O_4 @3DGF@NF and ZnCo_2O_4 @NF composites, respectively. With regard to the electrode prepared using the collected ZnCo_2O_4 powders, the powders were mixed with the conductive carbon black (Super P) and polymer binder (polyvinylidene fluoride) in a weight ratio of 8 : 1 : 1 in *N*-methyl-2-pyrrolidone (NMP) under a magnetic stirring for 24 h to form a homogeneous slurry, and then coated on a copper foil substrate and dried in a vacuum drying oven at 80 °C for 24 h. The average weight of the active materials was about 0.8–1.0 mg. Galvanostatic cycle performances of the



Scheme 1 Schematic illustration of the synthesis of ZnCo_2O_4 @3DGF@NF composites.

composite materials were measured at room temperature on a battery test system (Shenzhen Neware Battery, China) with a cutoff voltage of 0.01–3.0 V *versus* Li/Li⁺. The rate capabilities of the electrodes were measured at different current densities from 500 up to 4000 mA g⁻¹. Cyclic voltammetry (CV) was tested on an electrochemical workstation (CHI660D, China) at a scan rate of 0.5 mV s⁻¹ in a voltage range of 0.01–3.0 V (*vs.* Li/Li⁺). Electrochemical impedance spectroscopy (EIS) measurements were carried out in a frequency range of 100 kHz to 0.1 Hz on the CHI660D electrochemical workstation with a potential amplitude of 5 mV.

Results and discussion

Morphology and structural analysis

The composition and phase purity of ZnCo₂O₄ grown on graphene film coated on Ni foam are examined *via* X-ray diffraction (XRD). Fig. 1a shows the XRD pattern of the ZnCo₂O₄ powders, which are scratched from ZnCo₂O₄@3DGF@NF composite material so as to eliminate the strong impact of Ni foam substrate upon the XRD result. To get enough powders for experiments, we used the larger area 3DGF@NF as substrate and put two pieces of substrate in the same autoclave to grow ZnCo₂O₄ in the same concentration, then we can get powders by a long-period ultrasonication. Through repeated work we can finally collect enough powders for test. The observed diffraction peaks at 2θ values of 18.96°, 31.22°, 36.81°, 38.49°, 44.74°, 59.28°, 65.15° are well indexed to (111), (220), (311), (222), (400), (511), (440) planes of the cubic spinel ZnCo₂O₄ crystalline structure (JCPDS card no. 23-1390). Beyond those, no other diffraction peaks can be found in the XRD pattern, suggesting a successful synthesis of ZnCo₂O₄ materials with a high level of purity.

In order to clarify the property of deposited graphene substrate, the Raman spectrum of the 3DGF@NF and ZnCo₂O₄@3DGF@NF are investigated and demonstrated in Fig. 1b, respectively. It is obvious that no identifiable D band can be distinguished from the spectrum, implying that a high quality of graphene film with few defects was prepared. Furthermore, the Raman intensity of 2D band is lower than that of G band,

indicating that our synthesized graphene materials are actually composed of multilayered graphene sheets, which may result in good electronic conductivity.^{38,39} There is no significant difference in Raman spectrum between pre- and post- growing ZnCo₂O₄ on graphene, implying that the 3DGF kept an original structure and presented relatively robust stability.

The surface elements and their chemical states of the ZnCo₂O₄@3DGF@NF are analyzed *via* XPS, in order to further confirm the purity of ZnCo₂O₄. The overall surveyed spectrum (Fig. 2a) exhibits the presence of C, O, Co, Zn without other impurities. All of the high-resolution spectrums were fitted by the Lorentzian/Gaussian function in terms of spin-orbit doublets and shakeup satellites. Fig. 2b shows the high-resolution Zn 2p spectrum, and two peaks with binding energy values of 1021.3 eV and 1044.3 eV are ascribed to Zn 2p_{3/2} and Zn 2p_{1/2}, respectively, indicating the Zn(II) oxidation state in ZnCo₂O₄@3DGF@NF.⁴⁰ As indicated in Fig. 2c, the two strong peaks located at 779.9 eV and 794.8 eV are assigned to Co 2p_{3/2} and Co 2p_{1/2}, respectively, confirming the Co(III) oxidation state of ZnCo₂O₄@3DGF@NF.²¹ With respect to the high-resolution spectrum in the O 1s region (Fig. 2d), two peaks at 529.5 eV and 531.2 eV, were generally owed to the lattice oxygen and the oxygen in hydroxide ions, respectively.¹² The additional peak at *ca.* 533.0 eV should be generated from a small amount of physically adsorbed water molecules.⁴⁰ These results confirm that the valences of Zn, Co and O elements are +2, +3, and -2, respectively, which are corresponding to the element chemical states in ZnCo₂O₄ compound.

The morphology and detailed microstructure of graphene coated on Ni foam and ZnCo₂O₄ grown on 3DGF@NF substrate are characterized by FESEM, respectively. As depicted in Fig. 3a, it is obvious that the whole surface of Ni foam is covered with typical wrinkled graphene sheets. Then Fig. 3b reveals that the sheet-like ZnCo₂O₄ arrays are densely grown on the graphene substrate through hydrothermal route. Correspondingly, a closer observation seen from Fig. 3c finds that these ZnCo₂O₄ nanosheets are interconnected each other, which should be beneficial for ion and electron transport in the composite electrode. In addition, enough open space among sheets could be observed, which may facilitate the electrolyte penetration

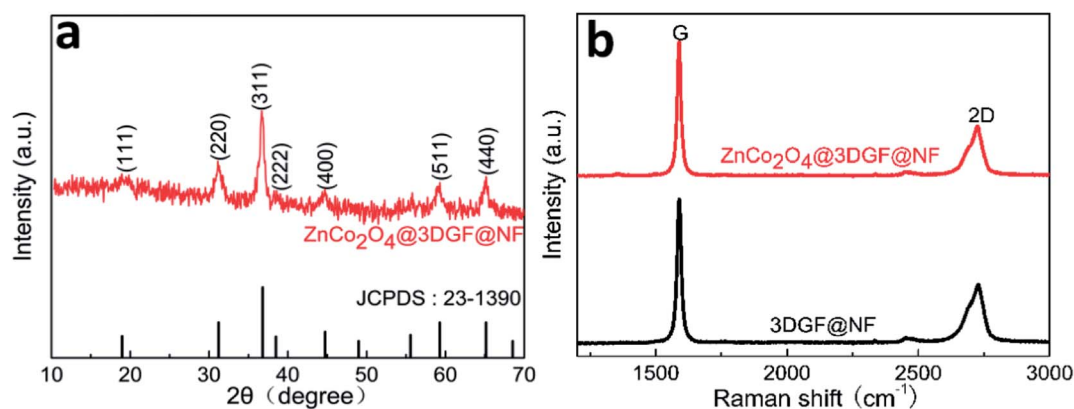


Fig. 1 (a) XRD pattern of ZnCo₂O₄ powders peeled from ZnCo₂O₄@3DGF@NF composite material; (b) Raman spectrum of 3DGF@NF and ZnCo₂O₄@3DGF@NF.

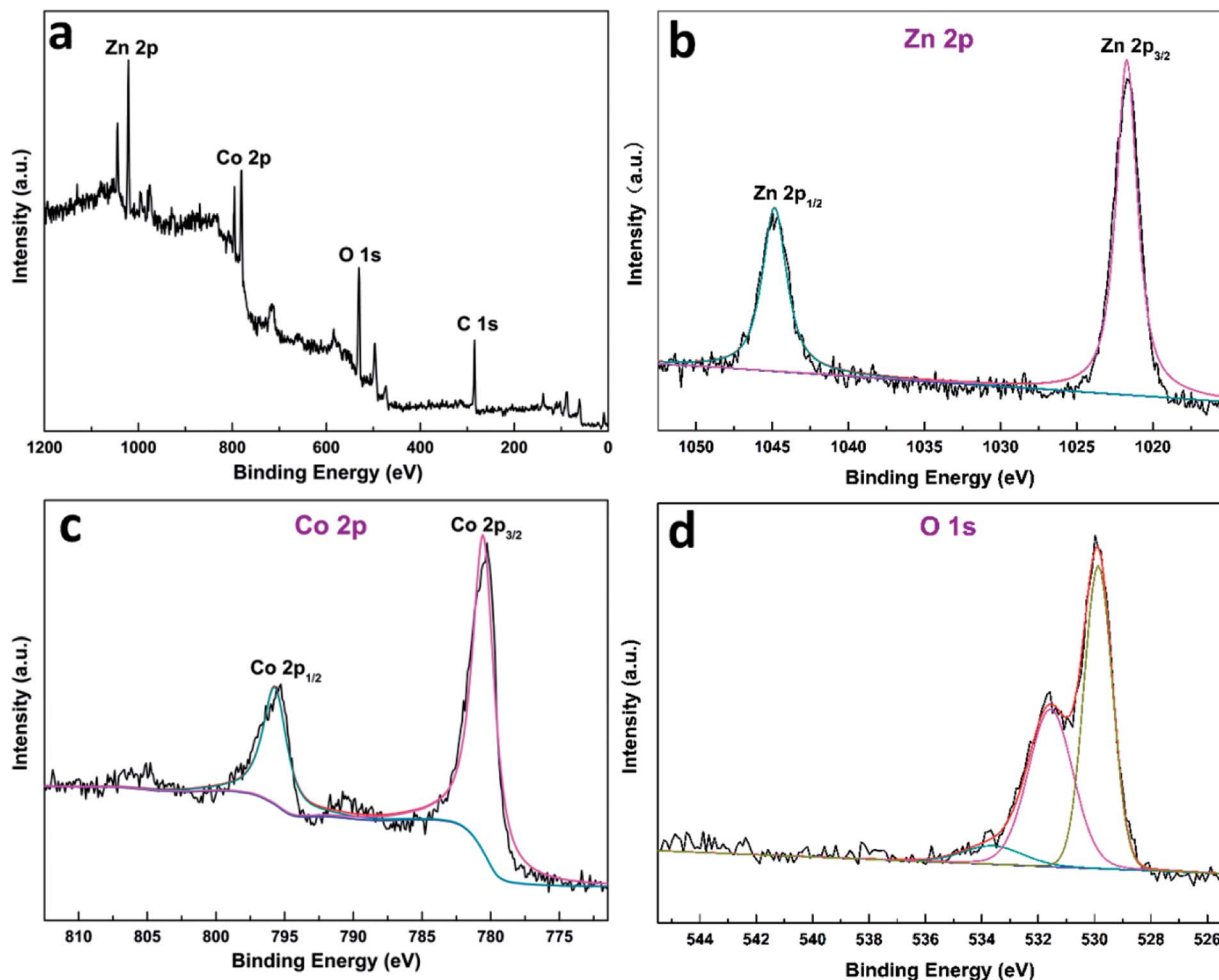


Fig. 2 XPS spectrum of (a) survey spectrum, (b) the Ni 2p, (c) the Co 2p and (d) the O 1s state in $\text{ZnCo}_2\text{O}_4@3\text{DGF@NF}$.

into the inner region of the electrode, increase the utilization of the active materials, as well as accommodate the volume expansion upon Li insertion. Additionally, it could be estimated from SEM images of Fig. 3c and d that the corresponding width of the ZnCo_2O_4 nanosheets ranges from 0.2 to 2 μm , the average thickness is approximately 20 nm. The composition and distribution of different elements in $\text{ZnCo}_2\text{O}_4@3\text{DGF@NF}$ are further investigated by EDS. The mapping results display a homogeneous distribution of Zn, Co, O elements on the flake materials, which also support the conclusion that pure spinel ZnCo_2O_4 materials have been prepared. Similarly, the EDS data of ZnCo_2O_4 nanosheet arrays (Fig. S1†) exhibit the signals of Zn, Co, O with the weight ratio of 1 : 1.99 : 0.94 and the atomic ratio which nearly agrees with the element proportions of 1 : 2 : 4. In order to investigate the relation between synthesized ZnCo_2O_4 nanostructure and substrate material, the morphology of collected ZnCo_2O_4 powders grown in solution and ZnCo_2O_4 directly grown on the Ni foam are also surveyed, respectively. As demonstrated in Fig. S2a and b,† in the absence of substrate, the SEM images reveal that the ZnCo_2O_4 microspheres of about 5–10 μm in diameter are produced, which are self-assembled by numerous thin sheets. The disordered sheet-like ZnCo_2O_4

densely grown on the Ni foam substrate is observed in Fig. S2c and d,† in regard to the morphology of $\text{ZnCo}_2\text{O}_4@NF$. Based on the above investigation, it could be found that the morphology of self-assembled nanostructured ZnCo_2O_4 materials prepared through hydrothermal way is very dependent on the substrate material, although the exact same synthetic strategy is applied.

To further identify the morphology and character of the ZnCo_2O_4 , the transmission electron microscopy (TEM) is carried out on the ZnCo_2O_4 materials exfoliated from 3DGF@NF substrate by a long-period ultrasonication. A typical TEM image of ZnCo_2O_4 nanosheet arrays is shown in Fig. 4a, and it is speculated that the average width of the nanosheets is about 1 μm , which is consistent with the SEM observation. From the TEM image with higher magnification (Fig. 4b), actually, the ZnCo_2O_4 nanosheets are self-assembled by numerous interconnected nanoparticles having a diameter in the range of *ca.* 10 ~ 25 nm, which may greatly enhance the surface-to-volume ratio of the active materials. For good measure, numerous irregular pores with a diameter distribution in the range of 5–20 nm across the ZnCo_2O_4 sheet could be observed in the Fig. 4b, which favors the alleviation of stress caused by volume variation, as well as electrolyte penetration.

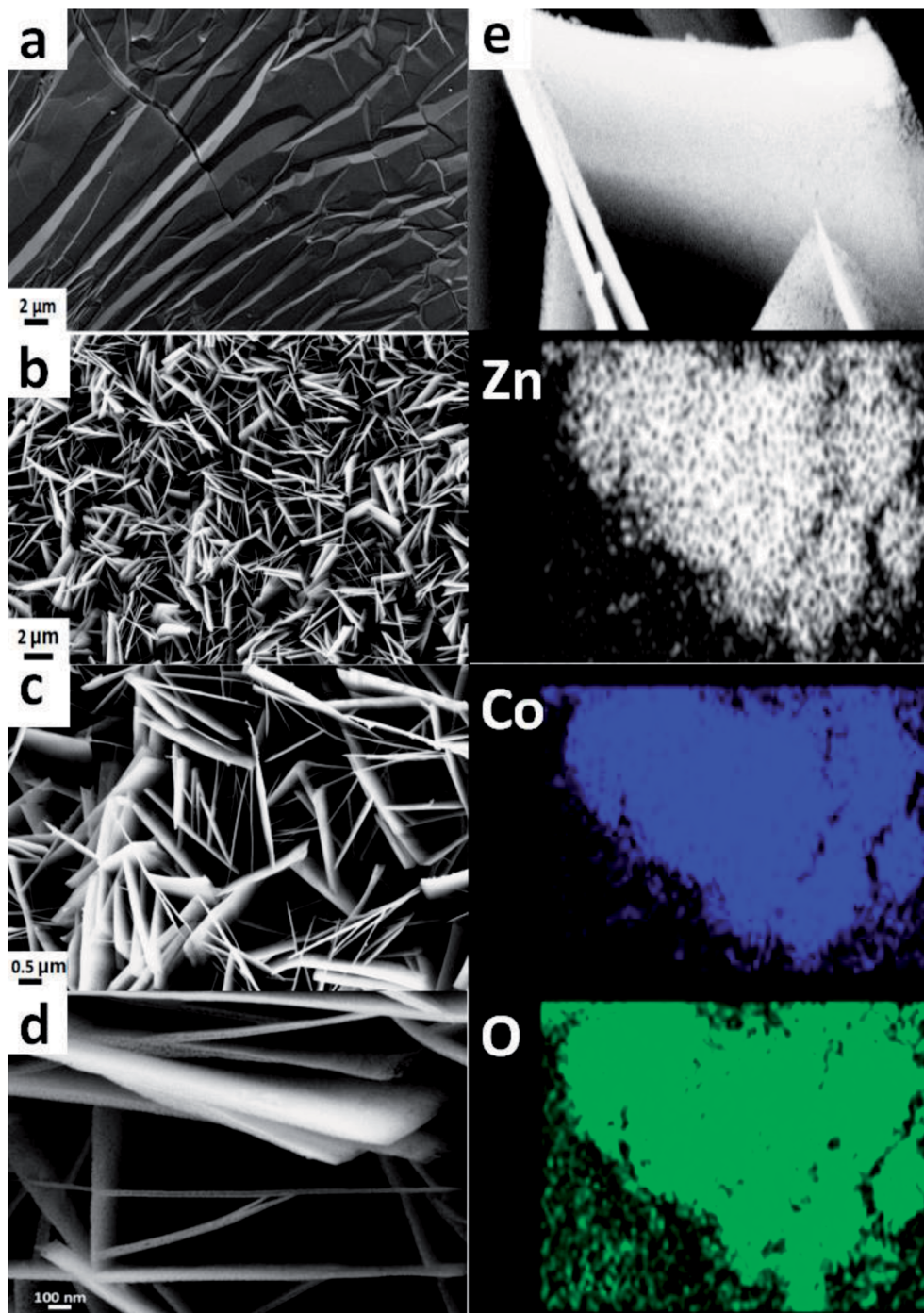


Fig. 3 (a) SEM image of pure 3DGF; (b–d) SEM images of $\text{ZnCo}_2\text{O}_4@3\text{DGF}@NF$ composites at different magnifications; (e) SEM image and corresponding EDS elemental mapping of Zn, Co and O for ZnCo_2O_4 nanosheet arrays.

The mesoporous structure observed in ZnCo_2O_4 sheets may be ascribed to the gas release (e.g. H_2O , CO_2) or H_2O lost during hydrothermal and the subsequent annealing processes.⁴¹ As shown in HRTEM image (Fig. 4c), the ZnCo_2O_4 nanosheets display different crystal orientation with clear lattice fringes, and the interplanar spacings can be estimated to be ~ 0.29 nm, ~ 0.25 nm, ~ 0.19 nm, which corresponds well to the distances of (220), (311), (400) planes of ZnCo_2O_4 phase, respectively. The corresponding selected area electron diffraction (SAED) pattern

(Fig. 4d) can be readily indexed to the (400), (311), (220) planes of the ZnCo_2O_4 crystal structure, which confirms the polycrystalline structure of the obtained ZnCo_2O_4 and is also in good agreement with the XRD results.

The N_2 adsorption–desorption measurement (Fig. 5) is carried out to investigate the specific surface area and the pore size distribution of $\text{ZnCo}_2\text{O}_4@3\text{DGF}@NF$ composite material by using Brunauer–Emmett–Teller (BET) method. First of all, we have to peel off the ZnCo_2O_4 nanosheets from the composite

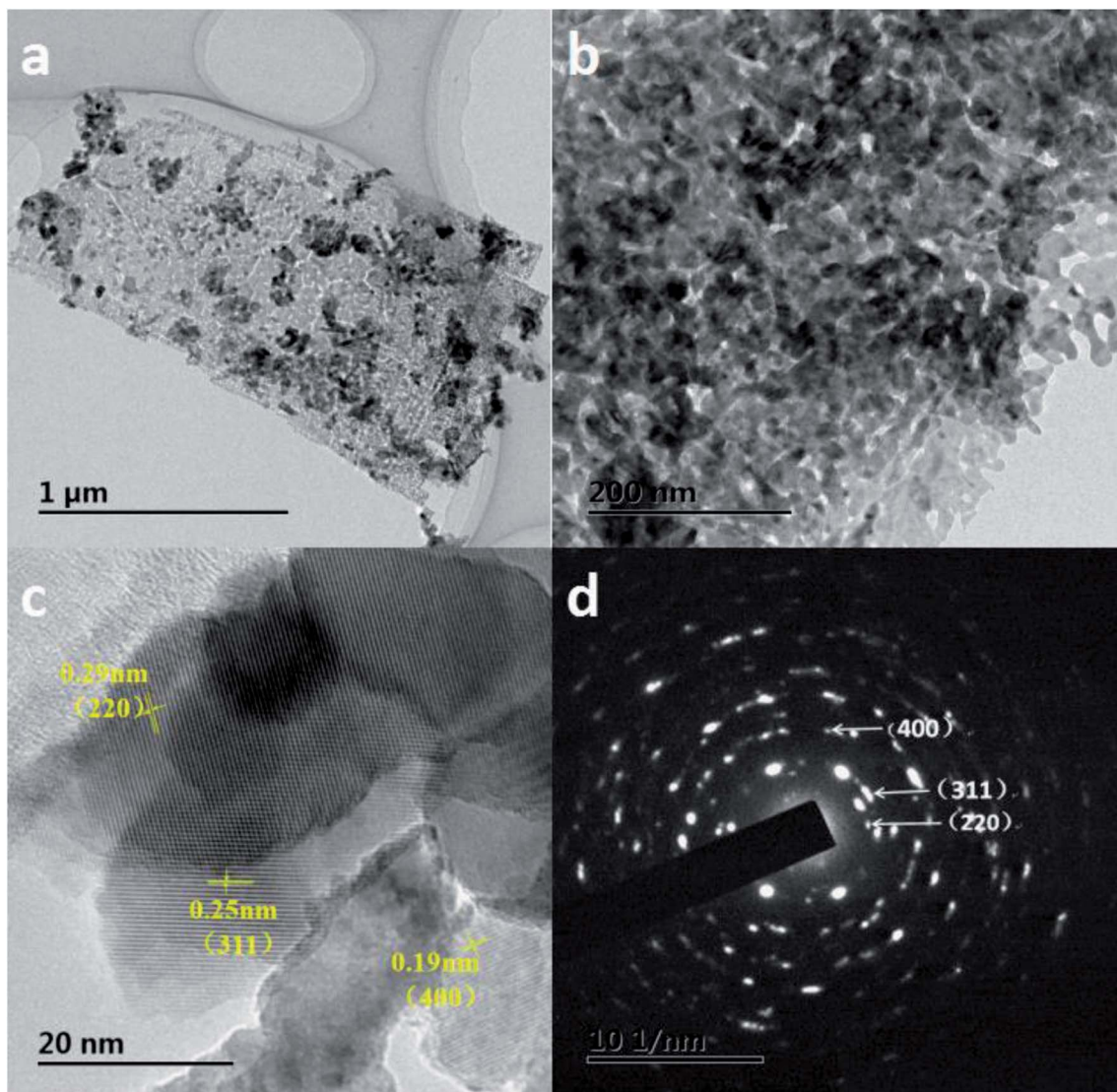


Fig. 4 (a and b) TEM images of the ZnCo_2O_4 nanosheet arrays; (c) HRTEM image of the ZnCo_2O_4 nanosheet arrays; (d) the corresponding SAED pattern.

electrode through a long-period ultrasonication. The isotherm profile for the $\text{ZnCo}_2\text{O}_4@3\text{DGF}@NF$ can be classified as type IV with a type H2 hysteresis loop observed in the range of 0.8–1.0 P/P_0 , indicating that the ZnCo_2O_4 nanosheets grown on graphene has a mesoporous structure. According to the corresponding Barrett–Joyner–Halenda (BJH) plots shown in the inset of the image, the pore size distribution is centered at 17.08 nm, which is consistent well with the TEM results and further proves the existence of mesoporous nature. Based on the measurement, the BET specific surface area and total pore volume of ZnCo_2O_4 grown on 3DGF are as high as $46.064 \text{ m}^2 \text{ g}^{-1}$ and $0.3684 \text{ cm}^3 \text{ g}^{-1}$, respectively. This mesoporous structure with high specific surface area can endow the $\text{ZnCo}_2\text{O}_4@3\text{DGF}@NF$ with more active sites for Li^+ insertion/extraction and space for the electrolyte penetration. Furthermore, the sufficient pore volume may accommodate the volume changes during lithiation/delithiation process, which may avoid the pulverization of the electrode.

Electrochemical evaluation of lithium ion batteries

The cyclic voltammetry (CV) and galvanostatic charge-discharge measurements are conducted to examine the electrochemical performance of the $\text{ZnCo}_2\text{O}_4@3\text{DGF}@NF$ electrode. Fig. 6a presents the initial three continuous cyclic voltammograms (CV) of $\text{ZnCo}_2\text{O}_4@3\text{DGF}@NF$ electrode at a scan rate of 0.5 mV s^{-1} . Noted that the CV curves show some extra cathodic/anodic peaks below 0.31 V, which may belong to the lithiation/delithiation process of the graphene substrate.³⁹ To verify this, we also test the first three CV curves of pure 3DGF@NF shown in Fig. S3†. It is obvious that the part below 0.31 V of CV curves in Fig. S3† is in accord with the CV plots of $\text{ZnCo}_2\text{O}_4@3\text{DGF}@NF$ electrode. In the first cycle of CV plots, two cathodic peaks are corresponding to the potential of ca. 0.31 V and 0.75 V. The sharp peak (ca. 0.75 V) can be assigned to the reduction process of ZnCo_2O_4 to metallic Zn and Co, while the broad peak (0.31 V) is correlated to the formation of a Li–Zn alloy, accompanied with the formation of a solid electrolyte

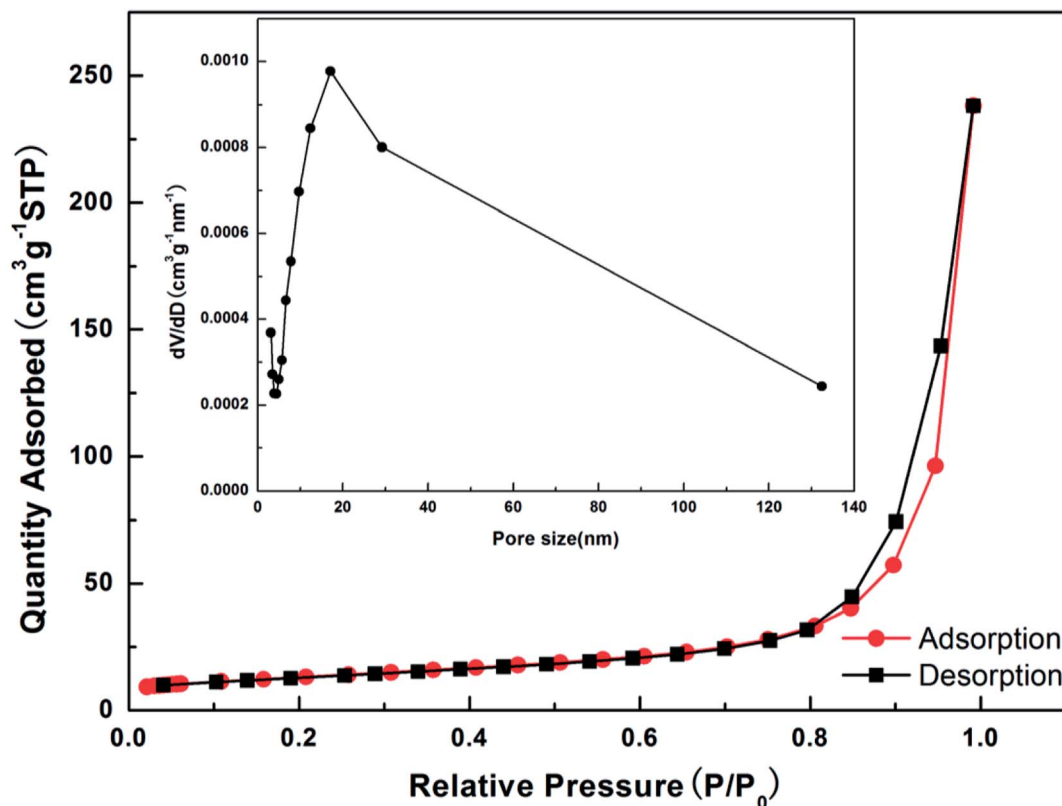


Fig. 5 N_2 adsorption/desorption isotherm and the inset corresponding to BJH pore size distribution of $ZnCo_2O_4@3DGF@NF$ composites.

interface (SEI) layer, which is caused by the decomposition of organic electrolyte.^{20,42} In the first anodic process, the oxidation peaks are observed at 0.7 V, 1.66 V, 2.26 V, respectively, which can be ascribed to Li–Zn dealloying reaction, the oxidation reaction and formation of ZnO and Co_3O_4 , respectively.²⁰ The discharge-branch voltammogram for the initial cycle is substantially different from those of the following ones, and in the subsequent scans, the reduction peak shifts to 1.1 V with a significant decrease in the peak intensity, revealing that an irreversible transformation and structure rearrangement have occurred. However, the subsequent curves overlap very well, reflecting a good reversibility of the electrochemical performances in the following circles.

According to the CV analysis and previous reports,^{19,43,44} the electrochemical reactions involved in the charge–discharge process are believed to proceed as follows:

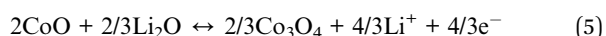
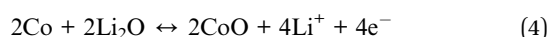
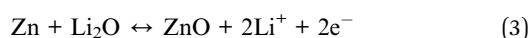


Fig. 6b shows the initial three charge–discharge profiles of the $ZnCo_2O_4@3DGF@NF$ electrode at a current density of

500 mA g^{-1} in the voltage window of 0.01–3.0 V (vs. Li/Li^+). It is noteworthy that in this work all the specific capacity and current density are calculated on the basis of the mass of $ZnCo_2O_4$ only, because the pure $3DGF@NF$ substrate demonstrates a rather low capacity (Fig. S4†) and makes very few contributions to the whole composite electrode. An obvious wide plateau between *ca.* 0.7 V and 1.0 V can be observed from the first discharge process, which attributes to the reduction of metal oxide to metal, accompanied with the Li_2O formation, while the subsequent discharge plateaus below 0.7 V should be assigned to the formation of the SEI film and Li–Zn alloy, which is in good agreement with CV results. The plateaus of subsequent discharge curves are slightly higher than the first cycle, which is also consistent well with the CV results. The initial discharge and charge capacities are 2024 and 1114 mA h g^{-1} , respectively, corresponding to a coulombic efficiency of *ca.* 55%. The large capacity loss of the electrode in the first cycle is due to the irreversible formation of a SEI layer, and the reduction of the electrolyte. What's more, the Li_2O produced during the first discharge process can only be partially decomposed and then react with Zn and Co nanoparticles *via* conversion reaction. The incomplete conversion reaction will cause the capacity loss, finally resulting in lower initial coulombic efficiency. In addition, the charge and discharge plateaus below 0.31 V can be also observed by this image, which is corresponding to the Li^+ de-intercalation and intercalation in graphene. This result is also consistent with the CV curves.

Fig. 6c displays the coulombic efficiency and cycling performance of the $ZnCo_2O_4@3DGF@NF$ electrode at a current

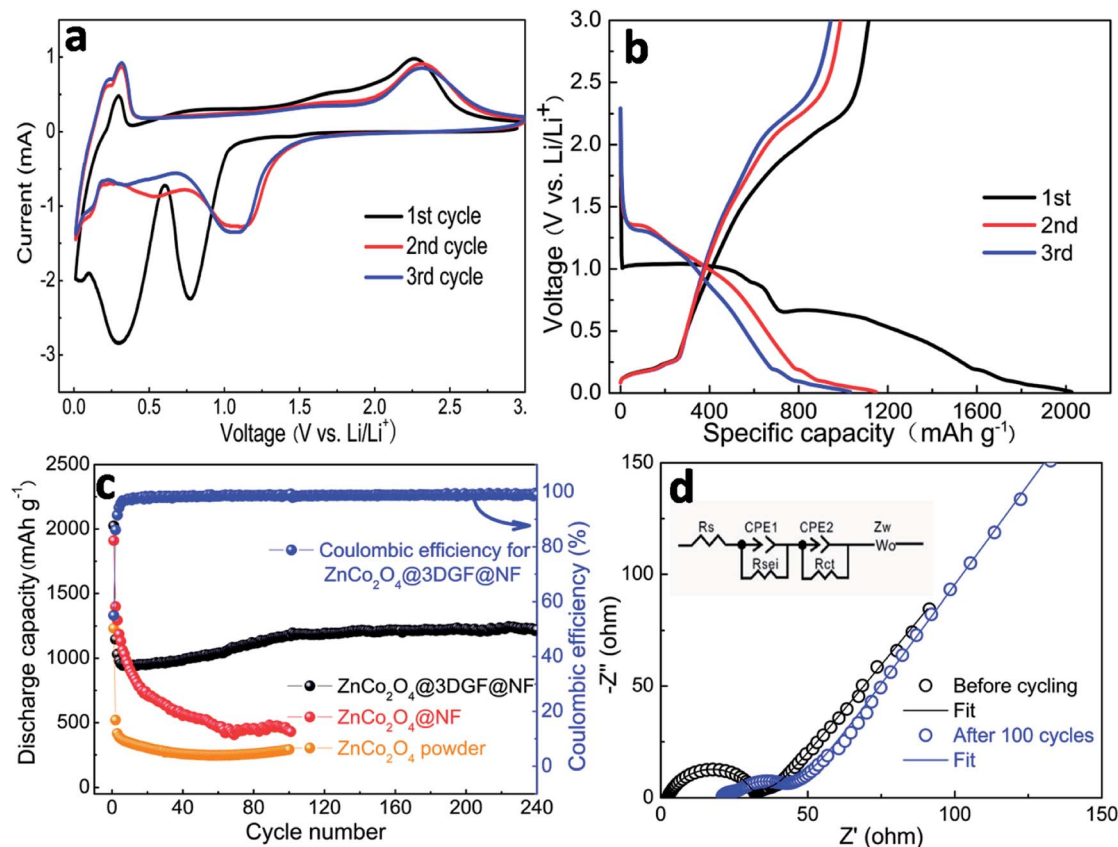


Fig. 6 (a) The first three cyclic voltammogram (CV) of the $\text{ZnCo}_2\text{O}_4@3\text{DGF@NF}$ electrode at a scan rate of 0.5 mV s^{-1} ; (b) galvanostatic charge–discharge profiles of the $\text{ZnCo}_2\text{O}_4@3\text{DGF@NF}$ electrode at a current density of 500 mA g^{-1} ; (c) comparison of cycle performance of the $\text{ZnCo}_2\text{O}_4@3\text{DGF@NF}$, $\text{ZnCo}_2\text{O}_4@NF$ and ZnCo_2O_4 powder electrodes at a current density of 500 mA g^{-1} ; (d) electrochemical impedance spectra (EIS) of the $\text{ZnCo}_2\text{O}_4@3\text{DGF@NF}$ electrode before and after 100 cycles.

density of 500 mA g^{-1} in a voltage window of $0.01\text{--}3.0 \text{ V}$ (vs. Li/Li^+). Although the initial coulombic efficiency is only *ca.* 55.0%, it increases rapidly and then stably maintains at a high level of *ca.* 97–99%, manifesting an admirable reversibility of this electrode. A lowest discharge capacity of 943 mA h g^{-1} is observed for the 14th cycle, and then gradually increases to 1176 mA h g^{-1} after 100 cycles. This special electrochemical performance is prevailing in MTMOs electrode materials, which may be attributed to the reversible growth and dissolution of a gel-like polymer film due to the kinetically activated electrolyte degradation.^{12,45,46} Finally, 1223 mA h g^{-1} is obtained for the $\text{ZnCo}_2\text{O}_4@3\text{DGF@NF}$ electrode after 240 cycles. For comparison, the cycling performances of $\text{ZnCo}_2\text{O}_4@NF$ electrode and electrode prepared using ZnCo_2O_4 powder are performed, respectively. After 100 cycles, the discharge capacity decreases to 430 and 291 mA h g^{-1} for $\text{ZnCo}_2\text{O}_4@NF$ and ZnCo_2O_4 powder electrodes, respectively, although they also have high initial discharge capacities of 1910 and 1232 mA h g^{-1} , respectively. The rapid capacity decay of the powder electrode should be attributed to the serious electrode pulverization caused by the volume changes during prolonged charge–discharge processes. In addition, although the capacity fading of the binder-free electrode of ZnCo_2O_4 directly grown on Ni foam is retarded, the cycling performance is still disappointing. These results

indicate that a smart design of electrode structure, and especially the 3DGF are indispensable for the superior cycling performance of ZnCo_2O_4 electrodes. The addition of graphene only contributes a very small proportion of overall capacity, but the graphene layers can enable effective strain relaxation of the whole composite electrode during cycling. Furthermore, the conductive 3DGF may result in excellent electrical conductivity. The synergistic effect of ZnCo_2O_4 and 3DGF is benefit for the whole composite electrode to exhibit superior electrochemical performance. As presented in Table S1,[†] the $\text{ZnCo}_2\text{O}_4@3\text{DGF@NF}$ electrode shows a relative low initial coulombic efficiency in these ZnCo_2O_4 based electrodes, but the coulombic efficiency can increase rapidly and then stably keep a high level of 97–99%. Through comprehensive analysis and evaluation, the long cycling life and remarkable reversible capacity can be obtained at a high current density in this work, which means this electrode is still superior to some of earlier reported ZnCo_2O_4 based electrodes.

The EIS measurements of the $\text{ZnCo}_2\text{O}_4@3\text{DGF@NF}$ electrode are performed before cycling and after 100 cycles at a current density of 500 mA g^{-1} . The inset is the equivalent circuit model. In this model, R_s is the internal resistance of the battery, R_{sei} and R_{ct} correspond to the SEI film and charge-transfer resistance, CPE1 and CPE2 are related to the

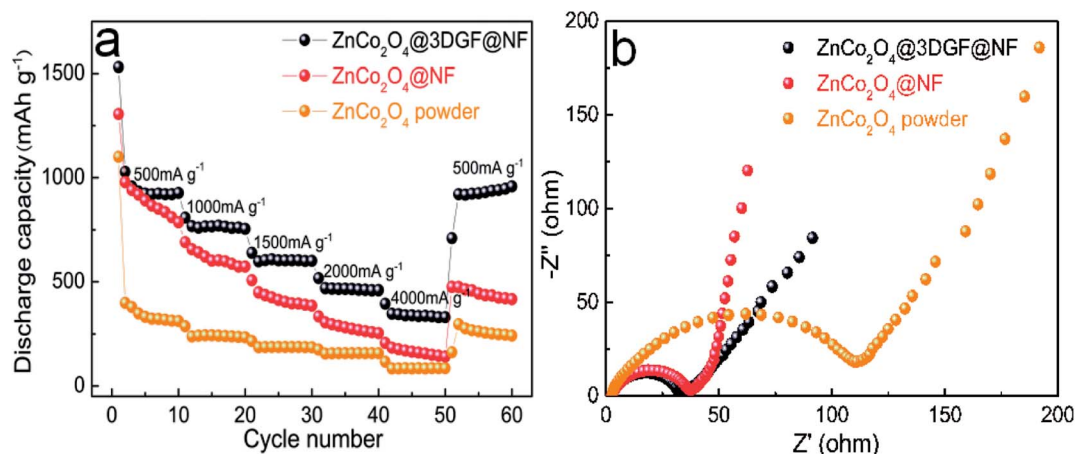


Fig. 7 (a) Rate performance and (b) EIS curves of the ZnCo₂O₄@3DGF@NF, ZnCo₂O₄@NF and ZnCo₂O₄ powder electrodes.

capacitance of SEI film and double layer capacitance, Z_w is the Warburg impedance. As shown in the Fig. 6d, both Nyquist plots are comprised of one semicircle at high frequency and a linear line at low frequency. The intercept of the semicircle on the real axis at high frequency is the resistance of electrolyte solutions, while the high frequency semicircle is assigned to the charge-transfer resistance. The semicircle diameter of ZnCo₂O₄@3DGF@NF electrode ($R_{ct} = 29.77 \Omega$) after 100 cycles is smaller than that of the fresh one ($R_{ct} = 30.31 \Omega$), indicating that the charge-transfer resistance has decreased after cycling. And the slope of the linear line of the cell after 100 cycles is a little steeper than that of the fresh one, indicating the Li ion diffusion kinetics have been improved after cycling. The enhanced Li ion diffusion kinetics and impaired charge-transfer resistance are benefited from the elaborate fabrication of the ZnCo₂O₄@3DGF@NF architecture, which can facilitate the electron and Li ion transmission.

The rate performance of electrodes is a critical parameter for high-power LIBs. As shown in Fig. 7a, the ZnCo₂O₄@3DGF@NF electrode exhibits a fairly stable rate performance at different current densities. When the current density increases step by step from 500 mA g⁻¹ to 1000, 1500, 2000, 4000 mA g⁻¹ for every 10 cycles, the corresponding discharge capacity is 927, 756, 603, 460, 331 mA h g⁻¹, respectively. After high rate cycles, the discharge capacity bounces back to 949 mA h g⁻¹ when the current density returns to 500 mA g⁻¹, which is even a little higher than that of the initial 10 cycles. This charge-discharge performance is also in accord with the increased specific capacity result. In comparison, the ZnCo₂O₄@NF and ZnCo₂O₄ powder electrodes both present terrible capacity fading at high current density and relatively poor rate performances shown in Fig. 7a. A better understanding of rate performance can be obtained from the EIS analysis. Fig. 7b displays the EIS curves of the fresh electrodes. Obviously, the charge-transfer resistances of ZnCo₂O₄@3DGF@NF and ZnCo₂O₄@NF are much smaller than the ZnCo₂O₄ powder electrode ($R_{ct} = 113.6 \Omega$), indicating that the binder-free electrode can effectively improve the electrochemical kinetic. Furthermore, the ZnCo₂O₄@3DGF@NF electrode ($R_{ct} = 30.31 \Omega$) demonstrates a lower resistance than the ZnCo₂O₄@NF electrode ($R_{ct} = 35.31 \Omega$), further confirming

that the 3DGF plays a crucial role in improving the electrochemical performance of the whole ZnCo₂O₄@3DGF@NF electrode.

In order to explain the excellent electrochemical performance of ZnCo₂O₄@3DGF@NF electrode, the SEM image of the fully charged ZnCo₂O₄@3DGF@NF electrode after 100 cycles is represented in Fig. 8. The interconnected nanosheets become curled after cycling, additionally the nanosheets get thicker due to the volume expansion after repeating charge-discharge process. However, the electrode still remains certain space between each nanosheet without collapsing, which is believed to accommodate volume changes during cycling and ensure the good structure stability of the electrode.

As discussed above, several beneficial factors attributes to the superior electrochemical performance of ZnCo₂O₄@3DGF@NF electrode. First, the binder-free electrode without the addition of conductive additive and polymer binder can avoid the side reaction, and enlarge the contact area between electrode-electrolyte. Second, the ZnCo₂O₄ directly grown on the current collector without milling can effectively prevent the nanomaterial agglomeration. Third, the unique mesoporous and sheet-like nanostructure is beneficial for electrolyte penetration, shortening of ion/electron transport distance. In addition, it is believed that the open spaces among nanosheets and

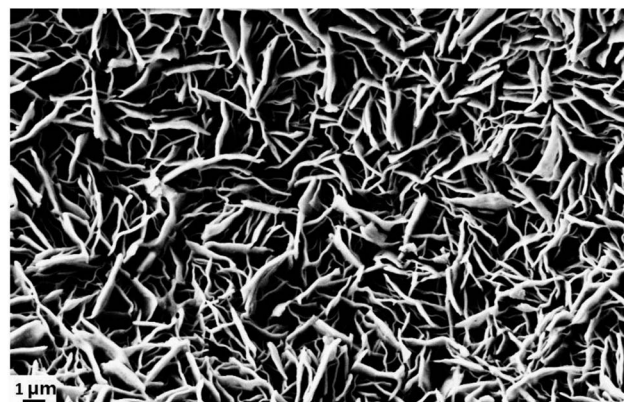


Fig. 8 SEM image of ZnCo₂O₄@3DGF@NF electrode after 100 cycles.

existed in mesoporous nanosheets can accommodate the volume variation. Last, 3DGF as a conductive substrate takes the advantages of high specific surface area, prominent electronic conductivity, and buffers the volume variation of electrode. In short, the synergistic effect of ZnCo₂O₄ nanosheet arrays and 3DGF leads to an outstanding electrochemical performance, demonstrating it can be a promising candidate of anode materials for LIBs.

Conclusions

In summary, we have successfully synthesized ZnCo₂O₄@3-DGF@NF as a binder-free electrode for LIBs by a simple hydrothermal method. Benefiting from the synergistic effect of ZnCo₂O₄ nanosheet arrays and 3DGF substrate, the binder-free electrode exhibits an excellent cycle performance (a discharge capacity of 1223 mA h g⁻¹ at the current density of 500 mA g⁻¹ after 240 cycles), rather stable rate capability and remarkable reversibility (coulombic efficiency of 97–99%), this nanostructure material shows a high electronic conductivity and stable mechanism property. There is no doubt that ZnCo₂O₄@3DGF@NF owns a great potential as the anode materials for high-performance LIBs.

Conflicts of interest

There are no conflicts to declare.

Acknowledgements

This work was financially supported by the National Science Foundation of China (61471317).

Notes and references

- 1 P. G. Bruce, *Solid State Ionics*, 2008, **179**, 752–760.
- 2 B. Scrosati and J. Garche, *J. Power Sources*, 2010, **195**, 2419–2430.
- 3 X. Chen, Y. Huang, T. Li, C. Wei, J. Yan and X. Feng, *Appl. Surf. Sci.*, 2017, **405**, 13–19.
- 4 Y. Ma, H. Tang, Y. Zhang, Z. Li, X. Zhang and Z. Tang, *J. Alloys Compd.*, 2017, **704**, 599–606.
- 5 L. Li, Y. Q. Zhang, X. Y. Liu, S. J. Shi, X. Y. Zhao, H. Zhang, X. Ge, G. F. Cai, C. D. Gu, X. L. Wang and J. P. Tu, *Electrochim. Acta*, 2014, **116**, 467–474.
- 6 L. Lu, H.-y. Wang, J.-G. Wang, C. Wang and Q.-C. Jiang, *J. Mater. Chem. A*, 2017, **5**, 2530–2538.
- 7 W. Wei, G. Oltean, C.-W. Tai, K. Edström, F. Björefors and L. Nyholm, *J. Mater. Chem. A*, 2013, **1**, 8160.
- 8 X. Yue, W. Sun, J. Zhang, F. Wang and K. Sun, *J. Power Sources*, 2016, **329**, 422–427.
- 9 Q. He, S. Gu, T. Wu, S. Zhang, X. Ao, J. Yang and Z. Wen, *Chem. Eng. J.*, 2017, **330**, 764–773.
- 10 Y. Huang, Z. Xu, J. Mai, T.-K. Lau, X. Lu, Y.-J. Hsu, Y. Chen, A. C. Lee, Y. Hou, Y. S. Meng and Q. Li, *Nano Energy*, 2017, **41**, 426–433.
- 11 J. Leng, Z. Wang, X. Li, H. Guo, T. Li and H. Liang, *Electrochim. Acta*, 2017, **244**, 154–161.
- 12 L. Zhan, S. Wang, L.-X. Ding, Z. Li and H. Wang, *Electrochim. Acta*, 2014, **135**, 35–41.
- 13 X. Hou, S. Bai, S. Xue, X. Shang, Y. Fu and D. He, *J. Alloys Compd.*, 2017, **711**, 592–597.
- 14 Z. Zhang, X. Zhang, Y. Feng, X. Wang, Q. Sun, D. Yu, W. Tong, X. Zhao and X. Liu, *Electrochim. Acta*, 2018, **260**, 823–829.
- 15 B. Qu, L. Hu, Q. Li, Y. Wang, L. Chen and T. Wang, *ACS Appl. Mater. Interfaces*, 2014, **6**, 731–736.
- 16 J. Yuan, C. Chen, Y. Hao, X. Zhang, S. Gao, R. Agrawal, C. Wang, Z. Xiong, H. Yu and Y. Xie, *J. Electroanal. Chem.*, 2017, **787**, 158–162.
- 17 M.-H. Jung, *Appl. Surf. Sci.*, 2018, **427**, 293–301.
- 18 A. K. Rai and J. Kim, *Solid State Sci.*, 2015, **48**, 90–96.
- 19 M. Zhen, X. Zhang and L. Liu, *RSC Adv.*, 2016, **6**, 43551–43555.
- 20 S. Hao, B. Zhang, S. Ball, M. Copley, Z. Xu, M. Srinivasan, K. Zhou, S. Mhaisalkar and Y. Huang, *J. Power Sources*, 2015, **294**, 112–119.
- 21 Q. Ru, D. Zhao, L. Guo, S. Hu and X. Hou, *J. Mater. Sci.: Mater. Electron.*, 2017, **28**, 15451–15456.
- 22 S. G. Mohamed, T.-F. Hung, C.-J. Chen, C. K. Chen, S.-F. Hu, R.-S. Liu, K.-C. Wang, X.-K. Xing, H.-M. Liu, A.-S. Liu, M.-H. Hsieh and B.-J. Lee, *RSC Adv.*, 2013, **3**, 20143.
- 23 M. Zhen, L. Liu and C. Wang, *Microporous Mesoporous Mater.*, 2017, **246**, 130–136.
- 24 Y. Zhu, C. Cao, J. Zhang and X. Xu, *J. Mater. Chem. A*, 2015, **3**, 9556–9564.
- 25 L. Hu, B. Qu, C. Li, Y. Chen, L. Mei, D. Lei, L. Chen, Q. Li and T. Wang, *J. Mater. Chem. A*, 2013, **1**, 5596.
- 26 C. Ding, X. Jiang, X. Huang, H. Zhang, W. Zhong, Y. Xia and C. Dai, *J. Alloys Compd.*, 2018, **736**, 181–189.
- 27 B. Liu, H. Liu, M. Liang, L. Liu, Z. Lv, H. Zhou and H. Guo, *Nanoscale*, 2017, **9**, 17174–17180.
- 28 X. Song, Q. Ru, B. Zhang, S. Hu and B. An, *J. Alloys Compd.*, 2014, **585**, 518–522.
- 29 Y. Pan, W. Zeng, L. Li, Y. Zhang, Y. Dong, D. Cao, G. Wang, B. L. Lucht, K. Ye and K. Cheng, *Nano-Micro Lett.*, 2016, **9**, 20.
- 30 G. X. Pan, X. H. Xia, F. Cao, J. Chen and Y. J. Zhang, *J. Power Sources*, 2015, **293**, 585–591.
- 31 T. Wang, Y. Guo, B. Zhao, S. Yu, H.-P. Yang, D. Lu, X.-Z. Fu, R. Sun and C.-P. Wong, *J. Power Sources*, 2015, **286**, 371–379.
- 32 Q.-Q. Ren, Z.-B. Wang, K. Ke, S.-W. Zhang and B.-S. Yin, *Ceram. Int.*, 2017, **43**, 13710–13716.
- 33 Q. Ren, C. Liu, Z. Wang, K. Ke, S. Zhang and B. Yin, *J. Nanosci. Nanotechnol.*, 2018, **18**, 1965–1969.
- 34 H. Wang, H. Feng and J. Li, *Small*, 2014, **10**, 2165–2181.
- 35 R. Raccichini, A. Varzi, S. Passerini and B. Scrosati, *Nat. Mater.*, 2015, **14**, 271–279.
- 36 X. Wu, S. Li, B. Wang, J. Liu and M. Yu, *RSC Adv.*, 2015, **5**, 81341–81347.
- 37 X. Wu, S. Li, B. Wang, J. Liu and M. Yu, *Phys. Chem. Chem. Phys.*, 2016, **18**, 4505–4512.
- 38 J. Luo, J. Liu, Z. Zeng, C. F. Ng, L. Ma, H. Zhang, J. Lin, Z. Shen and H. J. Fan, *Nano Lett.*, 2013, **13**, 6136–6143.

- 39 S. Liu, J. Wu, J. Zhou, G. Fang and S. Liang, *Electrochim. Acta*, 2015, **176**, 1–9.
- 40 H. S. Jadhav, A. Roy, W.-J. Chung and J. G. Seo, *Electrochim. Acta*, 2017, **246**, 941–950.
- 41 S. G. Mohamed, C. J. Chen, C. K. Chen, S. F. Hu and R. S. Liu, *ACS Appl. Mater. Interfaces*, 2014, **6**, 22701–22708.
- 42 G. Gao, H. B. Wu, B. Dong, S. Ding and X. W. Lou, *Adv. Sci.*, 2015, **2**, 1400014.
- 43 R. Zhao, Q. Li, C. Wang and L. Yin, *Electrochim. Acta*, 2016, **197**, 58–67.
- 44 B. Liu, J. Zhang, X. Wang, G. Chen, D. Chen, C. Zhou and G. Shen, *Nano Lett.*, 2012, **12**, 3005–3011.
- 45 J. Deng, L. Chen, Y. Sun, M. Ma and L. Fu, *Carbon*, 2015, **92**, 177–184.
- 46 J.-G. Wang, D. Jin, R. Zhou, C. Shen, K. Xie and B. Wei, *J. Power Sources*, 2016, **306**, 100–106.